

Electrostatic and Steric Interactions Determine Bacteriorhodopsin Single-Molecule Biomechanics

Kislon Voitchovsky, Sonia Antoranz Contera, and J. F. Ryan

Bionanotechnology Interdisciplinary Research Collaboration, Department of Physics, Clarendon Laboratory, University of Oxford, Oxford, United Kingdom

ABSTRACT Bacteriorhodopsin (bR) is a haloarchaeal membrane protein that converts the energy of single photons into large structural changes to directionally pump protons across purple membrane. This is achieved by a complex combination of local dynamic interactions controlling bR biomechanics at the submolecular level, producing efficient amplification of the retinal photoisomerization. Using single molecule force spectroscopy at different salt concentrations, we show that tryptophan (Trp) residues use steric specific interactions to create a rigid scaffold in bR extracellular region and are responsible for the main unfolding barriers. This scaffold, which encloses the retinal, controls bR local mechanical properties and anchors the protein into the membrane. Furthermore, the stable Trp-based network allows ion binding to two specific sites on the extracellular loops (BC and FG), which are involved in proton release and lateral transport. In contrast, the cytoplasmic side of bR is mainly governed by relatively weak nonspecific electrostatic interactions that provide the flexibility necessary for large cytoplasmic structural rearrangements during the photocycle. The presence of an extracellular Trp-based network tightly enclosing the retinal seems common to most haloarchaeal rhodopsins, and could be relevant to their exceptional efficiency.

INTRODUCTION

One of the most important challenges in biophysics is to understand how the protein amino-acid (aa) sequence relates to the local forces that dynamically control its structure and function. The exceptional efficiency characterizing most proteins relies on complex molecular biomechanics, featuring intricate combinations of different molecular interactions. Atomic force microscopy (AFM) is one of the most powerful techniques to address this problem because of its ability to directly investigate the local properties of single proteins in a nativelike environment and to quantify the magnitude of the key molecular interactions that determine their structure and function. Mechanical unfolding of individual proteins with AFM reveals sawtooth-shaped force-displacement curves that reflect the successive unfolding barriers (1–4). The characteristics of these patterns can be related to the protein inter and intramolecular interactions. However, unambiguous correspondence between unfolding barriers and specific molecular interactions relevant for the protein function is often difficult to establish, mainly because little information is available about the physical nature of the barriers. Several studies have successfully gained such information by investigating the dependency of the unfolding barriers on experimental parameters (5–7), but most of the single membrane protein unfolding AFM studies reported to date relate these barriers to general structural features like helix ends, breaks (3,4,8), and to interhelical hydrogen bonds (9,10). In this article, we show that bacteriorhodopsin (bR) unfolding pat-

terns depend on the medium ionic concentration and we identify the unfolding barriers remaining unaffected by ionic variations. This enabled us to directly relate the unfolding barriers to bR biomechanical properties and to the strategy adopted by the protein to function efficiently in extreme halophilic environments. Furthermore, our approach enables us to link the unfolding barriers to specific molecular interactions, and to observe single ion binding to the bR extracellular surface. Comparison of our results with those reported for halorhodopsin (8) supports our findings and suggests that bR molecular mechanical properties could be of importance to understand the outstanding efficiency with which archaeal rhodopsins convert the energy of a single photon into the large structural rearrangement leading to their various tasks.

bR is a light-driven proton pump naturally present in the purple membrane (PM) of *Halobacterium salinarum* (11). It occurs as trimers assembled in a hexagonal lattice with a variety of unusual membrane lipids (1:10 ratio) (12,13). bR is composed of seven *trans*-membrane α -helices (labeled A–G) enclosing a retinal chromophore linked to the G-helix via a Schiff base (14). Its robustness and structural similarity to G-coupled protein receptors (15) have made bR the most studied membrane protein; its atomic structure is known (14,16) and various techniques have resolved bR structural rearrangements during the photocycle (16–19). bR is the preferred model system for vectorial transport across the cell membrane. bR presents an extreme affinity for salt: *H. salinarum* thrives in 3–4 M NaCl solutions by maintaining an intracellular KCl concentration of ~ 3 M (20). bR exhibits an excess of acidic residues at its cytoplasmic surface (14,16), a characteristic of halophilic proteins (21,22), and PM lipids are highly branched and charged with archaeal tails (12,13). These

Submitted November 20, 2006, and accepted for publication May 8, 2007.

Address reprint requests to K. Voitchovsky, E-mail: k.voitchovsky1@physics.ox.ac.uk.

Editor: Anne S. Ulrich.

© 2007 by the Biophysical Society

0006-3495/07/09/2024/14 \$2.00

doi: 10.1529/biophysj.106.101469

features suggest that ion-mediated electrostatic interactions have important implications in bR structure and function (23).

Single molecule force spectroscopy has been extensively used to investigate the mechanical unfolding of soluble modular proteins (1,2,24–29) and membrane proteins (3,4,8,9,30,31). In contrast to soluble proteins for which the entropic loss induced by the protein extension is often sufficient to explain the energy dissipated in the unfolding process (1,32,33), an important part of the energy required to unfold a membrane protein arises from its anchoring to the membrane (34). Unfolding pathways of bR have been previously studied under different conditions of pH and temperatures (5,7,9,10,35). The positions of the main unfolding barriers opposing the protein un/refolding have been proposed, showing that α -helices tend to unfold in pairs, and emphasizing the role of interhelical hydrogen bonds and extracellular loops in bR stability (36). However, the complexity of the system still precludes a functional description of the interactions responsible for these barriers, and their relevance in bR local mechanical properties has never been addressed. Importantly, the role of salt ions in the unfolding barriers has not been examined. Previously, we showed that salt ions strongly affect protein-lipid and lipid-lipid electrostatic interactions within the PM cytoplasmic leaflet, but not the extracellular leaflet. This differential behavior is reflected in PM Young's modulus: the cytoplasmic leaflet is softer than the extracellular leaflet, and both leaflets harden with increasing salt concentration (23).

In this article we directly probe the influence of salt ions on bR intra- and intermolecular interactions by unfolding a single bR molecule from both its cytoplasmic and extracellular termini (C-terminus and N-terminus, respectively) at salt concentrations known to induce a differential stiffening of the membrane (20–40 mM KCl) (23). In this way, we are able to unambiguously isolate specific steric interactions from salt-dependent electrostatic contributions shaping bR unfolding patterns. The main unfolding barriers are steric, and lie within the stiff and rigid extracellular part of bR, providing specific ion binding sites identified on the extracellular loops by the unfolding curves. The cytoplasmic side is dominated by nonspecific ion-mediated electrostatic interactions that increase its structural flexibility. These results effectively relate the interactions determining bR structure, with the local mechanical properties and the force fields necessary to control bR activity.

MATERIALS AND METHODS

Purple membrane (PM) preparation

Deionized PM of *H. salinarium* (Sigma-Aldrich, Dorset, UK) was diluted in buffer (30 μ l of 10 mM Tris, 50 mM KCl, pH 8) and adsorbed on freshly cleaved mica (9.9 mm mica disks, Agar Scientific, Essex, UK). To avoid any possible misassembly of the PM lattice, the final experimental salt concentration was reached by further dilution with a buffer containing only Tris (pH 8) before imaging.

Single-molecule force spectroscopy of bR and PM imaging

Unfolding experiments were performed with an AFM MFP-3D (Asylum Research, Santa Barbara, CA) equipped with XYZ closed-loop feedback. No external oscillation was applied to the cantilever when unfolding bR (static mode). The approach speed was set to 200 nm/s. A dwell time of 1 s with the AFM tip pressing on the membrane with a constant given force (typically 1–2.5 nN) was allowed to favor nonspecific attachment of a protein terminus to the tip. To exclude possible tip-induced denaturation of the protein, the maximum pressing force exerted by the tip on the membrane was always <3 nN. The retraction speed was set to 100 nm/s to allow enough time for the attached protein to rearrange after possible tip-induced deformation while remaining fast enough to minimize thermal drift. The cantilever and the sample/buffer were regularly changed (typically every 500–800 unfolding attempts) to ensure reliability and reproducibility of the unfolding conditions. The side of the membrane on which the experiment was performed (cytoplasmic or extracellular) was identified before pulling by high resolution amplitude and phase imaging using amplitude-modulation AFM (AM-AFM) (23). Fig. 1 *a* presents an AM-AFM topograph of both PM surfaces in 30 mM KCl, 10 mM Tris, pH 8: PM cytoplasmic surface exhibits molecular resolution, but only bR trimers are resolved on the extracellular surface. The side assessment was always confirmed by the clear phase contrast between both PM surfaces and mica (Fig. 1 *b*) (23). The sample was imaged before and after pulling to ensure reliability of the unfolding curves. Both unfolding and imaging were done at $26 \pm 1^\circ\text{C}$ using TR400 silicon nitride cantilevers (Olympus, Tokyo, Japan) with nominal stiffness of 0.08 N/m. Cantilever stiffnesses were calculated using their thermal spectrum (38) and geometrical considerations (39). The error between the different calibration methods was typically within 10% of the nominal stiffness value.

Analysis of the unfolding curves

Fitting bR unfolding steps with the wormlike chain model equation (WLC) (33) allows the calculation of the protein's contour length L_{out} unfolded at each step. Fig. 2 illustrates the unfolding process for two successive steps and shows the corresponding distance L_{out} (Fig. 2, *b* and *c*). L_{out} provides an estimate of the corresponding number of aa extended out of the membrane (see Appendix A). We have applied the WLC model to fit each step of each bR unfolding curve. Using high resolution crystallographic models of the protein (14,16) it was possible to determine the particular location (along the protein aa sequence) of the unfolding barrier responsible for a given step (see Table 2, Fig. 2, and Appendix A for a detailed calculation example).

In principle, due to nonspecific binding of the AFM tip to the protein, each curve can represent an unfolding event carried out from a different aa of the bound terminus. Aligning the curves on a common step allows consistent statistics of the interstep distances (3,9) but every step position is shifted by an amount corresponding to the number of aa between the terminus extremity and the aa from which the protein is actually unfolded (see Appendix A). When unfolding bR from the C-terminus, we determined the tip-binding shift assuming that the first step observed (Fig. 3 *a*) corresponds to the position of the Lys²¹⁶ residue (see Appendix A). The binding shift of unfolding curves from the N-terminus was determined, assuming that the second step observed at low salt (~ 77 aa, see Fig. 3 *d*, see Table 2) is triggered by the extraction of Trp⁸⁰ (see Appendix A and Trp Residues Determine the Main Unfolding Steps through Specific Steric Interactions).

To avoid subjective interpretation of the data, the determination of the step positions, the fitting of the steps with the WLC model, and subsequent statistical analysis were carried out by special routines programmed using Igor Pro (Wavemetrics, Lake Oswego, OR) (Appendix B). An example of curve fits obtained using the routine is presented for each salt concentration studied in Fig. 4. Each step of each curve was analyzed and the results obtained were added up to form three-dimensional statistical histograms of the steps position (in aa extended outside the membrane) versus the corresponding extraction force and the corresponding frequency (see Fig. 1 *c*).

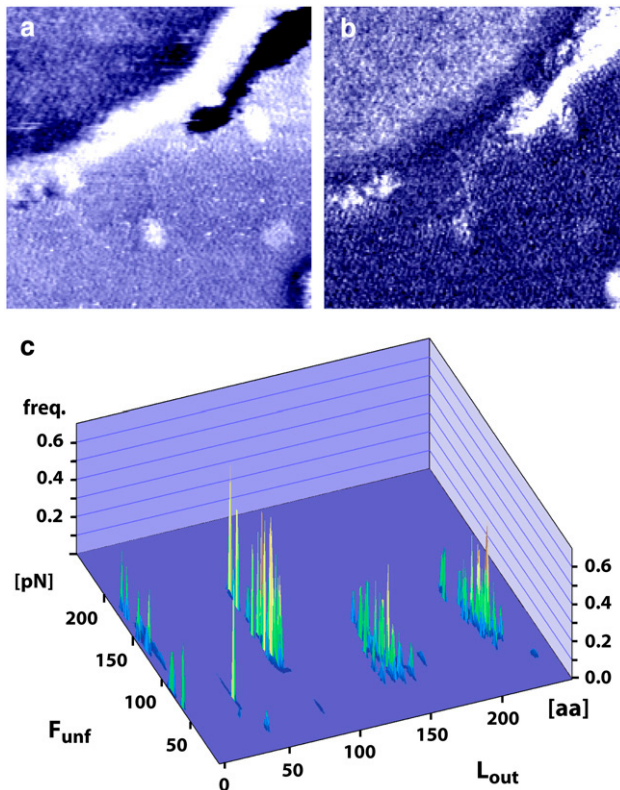


FIGURE 1 AM-AFM height (*a*) and phase image (*b*) of PM cytoplasmic (*lower*) and extracellular (*upper*) surfaces in liquid. Both images exhibit the well-known hexagonal bR lattice with the cytoplasmic surface allowing resolution of individual proteins while only trimers are visible on the extracellular surface. The side assessment is consistent with previously published high-resolution images of PM surface (84) and with the observed phase shift between the membrane two sides and the mica (23). The image was acquired immediately after several successful unfolding attempts on the membrane extracellular terminus, showing that the AFM tip is still clean. The size is 200×200 nm for both images. An example of three-dimensional statistical histogram obtained using the analysis software described in Materials and Methods is shown in panel *c*. F_{unf} is the unfolding force associated with a step corresponding to L_{out} aa extended outside of the membrane (see Fig. 2). The buffer is 30 mM KCl, 10 mM Tris-HCl at pH 8 for panels *a* and *b*, and 20 mM KCl, 10 mM Tris-HCl at pH 8 for panel *c*.

Each step is represented by a normalized two-dimensional Gaussian distribution. The Gaussian full width at half-maximum in both dimensions is determined by the WLC fit uncertainty (standard deviation) and the corresponding force uncertainty, respectively. The WLC histograms and the corresponding extraction forces presented in Fig. 3 are derived from the three-dimensional histograms data. Due to the reproducibility of bR unfolding patterns, the histograms exhibit local frequency maxima corresponding to particular bR extension lengths (see, e.g., Fig. 1 *c*). The maxima were fitted with Gaussian distributions at each salt concentration (Fig. 3 and Appendix B). The reliability of the different step attributions and the corresponding implications in the results interpretation are discussed in detail in Discussion and in Appendix C. For each histogram, the actual multi-Gaussian fitting was carried out using Igor Pro multipeak fitting package.

Forces statistics (see Fig. 3 and Table 2) were carried out over all the salt concentrations studied for a given step to increase the number of curves included in the statistics: a force profile was obtained for the considered step by integrating forces over the interval corresponding to the step location with

its standard deviation. The resulting force profile was then fitted with a Gaussian distribution (see Appendix B).

RESULTS

Single bR molecules were unfolded from their C- and N-termini at salt concentrations ranging from 20 to 40 mM KCl, always buffered with 10 mM Tris-HCl at pH 8. In each case a set of typically 30–50 complete unfolding events were recorded for both cytoplasmic and extracellular unfolding (see Table 1). Each set of curves was statistically analyzed (see Materials and Methods and Appendix B). Histograms representing the fit of the unfolding steps with the WLC model are presented in Fig. 3. For each set, a representative unfolding curve is also presented (Fig. 4) with the WLC fit of the steps. The unfolding barriers measured at the different ionic concentrations investigated are summarized in Table 2 with their respective corresponding unfolding force. Fig. 6 shows cartoon representations of the unfolding barriers reported in Table 2.

Unfolding bR from PM cytoplasmic side

Figs. 3 and 4, *a–c*, show the unfolding patterns obtained by extracting bR from its C-terminus at different salt concentrations. Only curves corresponding to a full unfolding of the protein were used (curves with the final force peak occurring beyond ~ 60 nm (3,9)).

At 20 mM KCl (Figs. 3 *a* and 4 *a*), most of the recorded cytoplasmic unfolding events show the characteristic unfolding pattern reported previously (four steps at ~ 5 nm, ~ 27 nm, ~ 43 nm, ~ 65 nm) (3,5,9,35). Each step is discrete and the unfolding pattern is reproducible as shown by the statistical histogram. The corresponding stretching forces are discussed below (see Unfolding Forces).

At 30 and 40 mM KCl, the four main steps are still present in the histograms (*blue Gaussian curves* in Fig. 3, *b* and *c*), but new peaks corresponding to ionic-dependent interactions gradually appear as the KCl concentration increases (*red and black Gaussian curves* for 30 and 40 mM KCl, respectively, in Fig. 3, *b* and *c*), reflecting an improved bR stability due to better shielding of bR intra- and intermolecular electrostatic repulsion (23). Since the tip can nonspecifically bind to several aa of the C-terminus, the curves were aligned for the histograms using their unfolding step located at ~ 25 nm away from the membrane (*third unfolding step* in Figs. 3 *a* and 4 *a*) (3,9).

Unfolding from PM extracellular side

Unfolding bR from the extracellular N-terminus (*extracellular curves*, Figs. 3 and 4, *d–f*) presents a different pattern from the C-terminus unfolding, and is generally more difficult to achieve. At 20 mM KCl (Figs. 3 *d* and 4 *d*) the extracellular unfolding patterns present four main steps (at ~ 5 nm, ~ 25 nm, ~ 40 nm, ~ 60 nm) corresponding to those reported

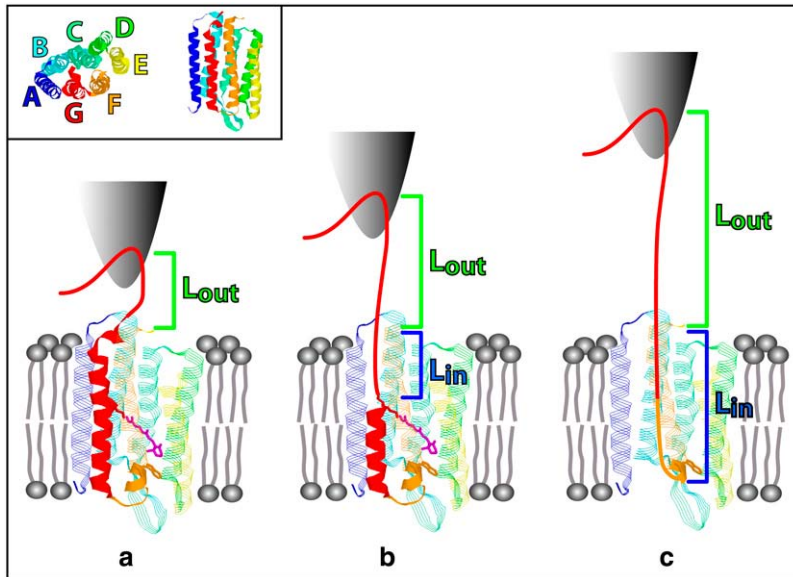


FIGURE 2 Unfolding principle. The AFM tip binds to bR cytoplasmic terminus (a). The tip starts to unfold the protein by stretching part of helix G up to a first unfolding barrier (Lys²¹⁶) (b). When the pulling force is sufficient, the barrier is overcome and the helix can be stretched up to the next unfolding barrier (Trp¹⁸⁹) (c). The effective protein length stretched is $L_{out} + L_{in}$ but the WLC only accounts for L_{out} . It is therefore necessary to know L_{in} (calculated from (14) and (16)) to accurately determine the unfolding barrier location (see Appendix A for a detailed example).

previously (10). The last step was sometimes doubled, with $\sim 35\%$ of the unfolding event showing an additional last step (Fig. 3 d).

At 30 and 40 mM KCl, the main steps mentioned above are still present, but new salt-dependent unfolding steps appear (Figs. 3 and 4, e and f). Similarly to cytoplasmic curves, the different unfolding barriers identified were fitted using Gaussian curves (same color code). All the extracellular curves retained were aligned using the second main step (~ 25 nm).

DISCUSSION

Tip-protein binding and unfolding mechanism

Experimentally, pressing with the tip on the membrane largely favors nonspecific attachment of single bR molecules to the AFM tip. The corresponding probability to bind a protein depends on the protein terminus targeted and on the medium ionic concentration (see Table 1): for a given force applied by tip to the membrane, the probability for bR-tip binding follows the leaflet-dependent increase of PM stiffness with salt concentration (23). This suggests that perturbing intramembrane interactions favors nonspecific tip-protein binding. The pressing forces employed (< 3 nN) should, however, only elastically deform the membrane, and the speed of the subsequent unfolding process (100 nm/s) is slow enough to allow sufficient time for the unfolded protein to rearrange before the first unfolding event occurs. Since the PM surface is highly charged (18,23), progressive ion shielding of electrostatic repulsion allows more interactions to stabilize the protein, making its unfolding more difficult. The efficiency of the unfolding can be related to the membrane stiffness at different salt concentrations:

1. At 20 mM KCl, the membrane is soft and presents a reduced Young's modulus E (typically $\sim 25\%$ of native

value) (23). The interactions maintaining PM structure are nonelectrostatic and specific, and appear to be located mainly in the extracellular leaflet (40,41) (Table 2, Fig. 3, a and d, and Fig. 6, a_C-e_C and a_E-e_E) for which E is substantially larger than in the cytoplasmic leaflet. Although it is easier to extract proteins from the softer cytoplasmic leaflet, the positively charged Arg⁷ residue interacting with the weakly negatively charged AFM tip (42) may assist tip binding to the extracellular terminus. Only the specific intra- and intermolecular interactions maintaining the membrane cohesion are responsible for the observed steps.

2. At 30 and 40 mM KCl, $E_{cyto}/E_{extracell}$ is bigger (> 0.6), allowing electrostatic contributions to appear in the unfolding curves, mainly corresponding to locations in the cytoplasmic leaflet (Fig. 6, f_C-p_C and f_E-m_E). Unfolding barriers on the extracellular loops can also be observed (Fig. 6, $f_C, j_C, m_C, o_C, h_E,$ and m_E). The specific contributions observed at low salt are still present (Fig. 3, b, c, e, and f).

Trp residues determine the main unfolding steps through specific steric interactions

Trp residues play an important role in bR stability (18,43,44) and activity (45–47) and are the only large bR residues located exclusively in PM extracellular leaflet (14,41) (see Fig. 5). Three of bR's eight Trp residues (Trp⁸⁶, Trp¹⁸², and Trp¹⁸⁹) point mostly toward the inside of the protein and compose part of the rigid retinal binding pocket (48–50) that controls and catalyzes the retinal photoisomerization process (43,47,51). Inside bR, the retinal photoisomerizes around its $C_{13} = C_{14}$ double bond; steric interactions between the pocket residues and the retinal are responsible for the stereospecific isomerization and

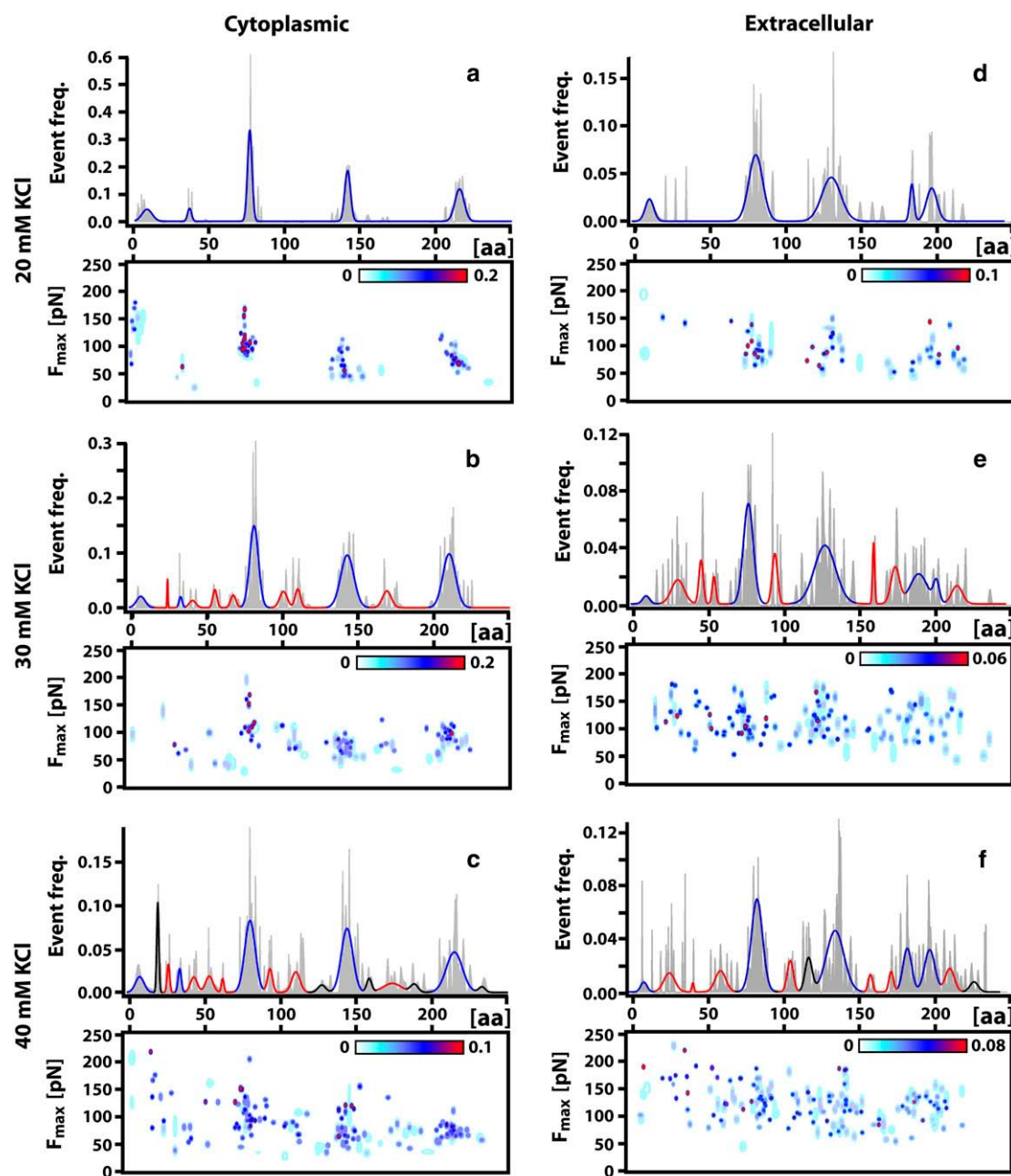


FIGURE 3 Histograms representing the number of aa extended out of the membrane with each unfolding step for the different salt concentrations studied (L_{out} in Fig. 2). The histograms were obtained from individual fitting of each curve unfolding steps with the WLC model (Fig. 4). The steps are represented by Gaussian curves which, at full width at half-maximum, correspond to the fitting standard deviation. Unfolding was carried out from bR C-terminus (a–c) and N-terminus (d–f) independently at each salt concentration investigated. The steps reported in Table 2 were obtained by fitting the histograms with Gaussian distributions. The Gaussian color represents the salt concentration at which the corresponding step has been first reproducibly observed (blue at 20 mM KCl, 10 mM Tris-HCl, pH 8; red at 30 mM KCl, 10 mM Tris-HCl, pH 8; and black at 40 mM KCl, 10 mM Tris-HCl, pH 8). For each histogram, the corresponding top view of a three-dimensional force plot is also presented (the color scale represents the frequency of the reported events).

for the high quantum efficiency (52–54), and the Trp present are believed to play an important role in the process (46,50,55). The other Trp residues (Trp¹⁰, Trp¹², Trp⁸⁰, partially Trp¹³⁷ and Trp¹³⁸) point more toward the outside of the protein (14,16). They are not directly involved in bR photoactivity (50) (apart

from Trp¹³⁷, (45)) but seem to rigidify the protein through a hydrogen-bond network (48,56) and are thought to anchor bR into PM (18,23).

Studies on model peptides flanked with Trp have demonstrated the importance of these bulky residues for anchoring

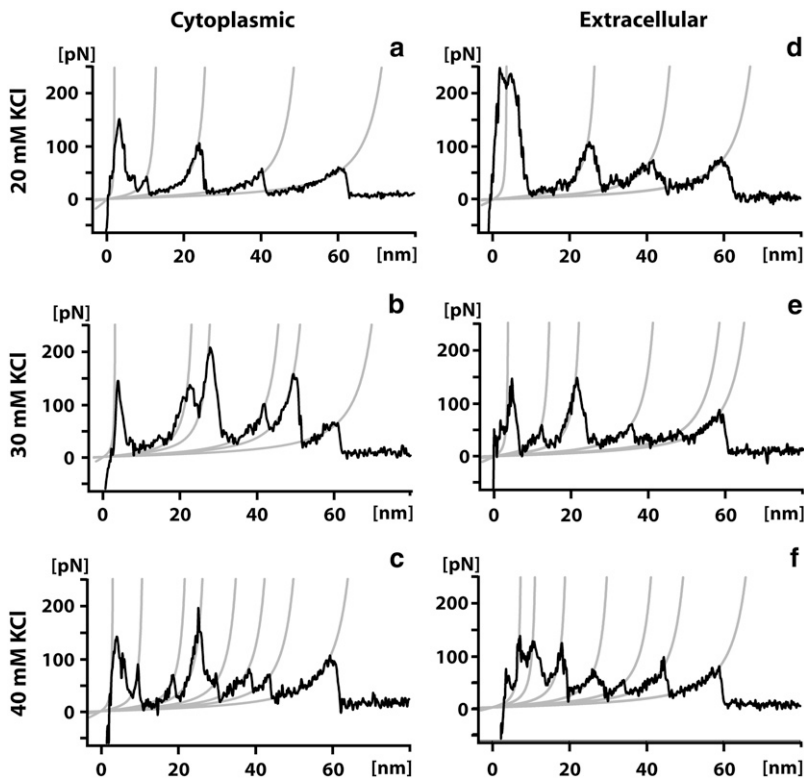


FIGURE 4 WLC fit (light shaded) of representative unfolding curves from bR C- and N-terminus (solid) for each salt concentration studied. The fits were obtained using the analysis procedure described in Appendix B. The notation used to designate the condition in which each unfolding curve presented was acquired is identical as in Fig. 3. All the KCl solutions are buffered with 10 mM Tris-HCl at pH 8.

the peptide into a lipid membrane (34,57,58) and have shown that hydrophobic interactions can be overcome by Trp-lipid interactions (59).

These results strongly suggest that the extraction of Trp residues is responsible for the main unfolding steps observed, especially at low salt where steric specific interactions dominate the membrane.

Unfolding from the C-terminus

When fitting cytoplasmic unfolding curves at 20 mM KCl with the WLC model (Figs. 3 and 4 a), the location obtained for each step can be interpreted by invoking resistance from a Trp (Table 2, Fig. 6, a_C – e_C). If the first step is assumed to correspond to the position of Lys²¹⁶ (see Materials and

Methods), the second step then coincides with the position of Trp¹⁸⁹. The third main step can be attributed to the extraction of Trp¹³⁷ and the fourth step to the anchoring of helix C in the membrane by Trp⁸⁰. The last step can be explained by the anchoring of helix A in the membrane by Trp¹⁰ and Trp¹².

Unfolding from the N-terminus

Trp residues can also explain the steps observed at low salt concentration on extracellular curves (Fig. 3 d, Table 2 and Fig. 6, a_E – d_E). Taking into account the tip-binding shift (determined using the second step, see Materials and Methods and Appendix A), the first step corresponds to the extraction of Trp¹⁰ and Trp¹². This step is present, however, in a low percentage of curves (27%) and with a large fitting uncertainty. This can be explained by the protein elastic deformation induced by the tip when pressing on the membrane. Since the N-terminus is relatively short, the actual unfolding process may begin before the tip has moved far enough from the membrane, thus affecting the first unfolding step. The second step is assumed to be triggered by the extraction of Trp⁸⁰ (see Appendix A). The hydrogen bond between Tyr⁸³ and Trp¹⁸⁹ (14) could also play a role for this step. The third step is attributed to Trp^{137–138}. The first part of the last step can then be attributed to Trp¹⁸⁹ while the second suggests the involvement of the F-G loop glutamates, namely Glu¹⁹⁴ and Glu²⁰⁴ (Table 2 and Fig. 6 e_E) (see Specific K⁺ Binding to the Glu^{74–75} and Glu^{194–204} Residues Located on bR Extracellular Interhelical Loops).

TABLE 1 Percentage of events representing a full unfolding of the protein at the different salt concentrations studied

KCl concentration	PM terminus pulled from	Number of full unfolding events (as % of attempts)
20 mM	C-terminus	38 (4.32%)
	N-terminus	31 (2.25%)
30 mM	C-terminus	35 (2.17%)
	N-terminus	49 (1.25%)
40 mM	C-terminus	42 (0.87%)
	N-terminus	41 (0.92%)

The protein is unfolded from both its termini at each ionic concentration investigated. As the salt concentration increases, the Young's moduli of both PM leaflets increase differentially (23). This is reflected by a decrease in the success rate when attempting to unfold the protein.

TABLE 2 Location of the unfolding barriers obtained from fitting with the WLC model and proposed corresponding event in the protein

Cytoplasmic				Extracellular			
Fig. 6	aa pos. of step	F_{unf} (pN)	Proposed corresponding aa/event in the protein	Fig. 6	aa pos. of step	F_{unf} (pN)	Proposed corresponding aa/event in the protein
20 mM KCl	a_C	8 ± 6	144 ± 29 Lys ²¹⁶ (tip binds: L230, M228)	a_E	7 ± 4	138 ± 57	Trp ¹⁰⁻¹² (L11, M12)
	b_C	35 ± 2	62 ± 17 Trp ¹⁸⁹ (L189, M187)	b_E	77 ± 7	111 ± 41	Trp ⁸⁰ (tip binds: L3, M3)
	c_C	80 ± 3	101 ± 23 Trp ¹³⁷⁻¹³⁸ (L142, M140)	c_E	129 ± 9	109 ± 44	Trp ¹³⁷⁻¹³⁸ (L132, M132)
	d_C	141 ± 3	64 ± 35 Trp ⁸⁰ , Tyr ⁸³ (L81, M79)	d_E	184 ± 2	65 ± 34	Trp ¹⁸⁹ (L188, M189)
	e_C	212 ± 5	73 ± 13 Trp ¹⁰⁻¹² (8L, 6M)	e_E	199 ± 5	106 ± 35	Glu ¹⁹⁴⁻²⁰⁴ (L201, M204)
30 mM KCl	f_C	22 ± 1	138 ± 9 Glu ¹⁹⁴ (L195, M195)	f_E	28 ± 6	143 ± 43	Asp ³⁶⁻³⁸ (L40, M41)
	g_C	39 ± 4	67 ± 14 Pro ¹⁸⁶ (helix F looping) (L184, M183)	g_E	45 ± 1	76 ± 20	Pro ⁵⁰ , (kink of helix B) (L53, M55)
	h_C	53 ± 1	95 ± 10 Extract Trp ¹⁸⁹ cyto. surf. (L175, M173)	h_E	57 ± 3	110 ± 30	BC loop Glu (L60, M60)
	i_C	65 ± 3	39 ± 8 Glu ¹⁶¹ , Arg ¹⁶⁴ , EF-loop (L163, M161)	i_E	92 ± 3	106 ± 15	Asp ¹⁰¹⁻¹⁰³ , Glu ¹⁰⁴ (L105, M106)
	j_C	97 ± 4	111 ± 11 Lys ¹²⁹ (L124, M124)	j_E	157 ± 1	89 ± 10	Glu ¹⁶⁶ , EF loop (L169, M170)
	k_C	109 ± 3	78 ± 13 Asp ¹¹⁵ , helix D looping (L116, M113)	k_E	174 ± 3	101 ± 47	Pro ¹⁸⁶ (helix F looping), Trp ¹⁸² (L180, M181)
	l_C	169 ± 4	73 ± 12 Pro ⁵⁰ (kink of helix B) (L53, M51)	l_E	212 ± 5	101 ± 44	Glu ²³¹⁻²³³⁻²³⁶ (L224, M223)
40 mM KCl	m_C	18 ± 1	168 ± 52 Glu ²⁰⁴ (L200, M200)	m_E	114 ± 4	91 ± 38	Lys ¹²⁹ (L121, M120)
	n_C	128 ± 3	44 ± 12 Asp ¹⁰¹⁻¹⁰³ (L102, M100)	—	225 ± 3	62 ± 35	C-terminus extraction
	o_C	154 ± 2	154 ± 16 BC loop Glu (L65, M64)				
	p_C	189 ± 3	78 ± 9 Asp ³⁶⁻³⁸ (L40, M39)				
	—	233 ± 3	59 ± 7 N-terminus extraction				

The labeling of the barriers is consistent with Fig. 6. At each salt concentration, only the new steps appearing in the unfolding curves are reported in the table but the steps measured at lower salt concentrations are still present (see Fig. 3). For each step, the number of amino acids extended out of membrane (L_{out} , see Fig. 2), the corresponding unfolding force and their respective standard deviations are displayed. The position of the corresponding unfolding barrier calculated using two structural models of bR (L) (14) and (M) (16) is also given with the proposed amino-acid/event responsible for the observed step. When pulling from PM cytoplasmic side (C-terminus), the last amino acid to which the tip attaches is determined assuming that the first step at low salt is triggered by Lys²¹⁶. For extracellular unfolding (N-terminus), the position of the tip attachment is determined assuming that Trp⁸⁰ is responsible for the second main step (Appendix A). The steps showing italicized force values could not be satisfactorily fitted with a Gaussian distribution due to significant force variations. For each force reported, if the standard deviation was smaller than the cantilever calibration error (10%), the latter value was used.

Considerations derived from thermally assisted bond rupture theory also support the role of steric interactions in the observed steps and suggest the responsibility of bulky residues; independent studies of bR unfolding have found that

the extraction force associated with the main steps decreases with increasing temperature (5), and increases linearly with the logarithm of the pulling speed (7), suggesting a stick-slip behavior (34). If Trp steric interactions are responsible for the unfolding steps, extracting these bulky residues from the membrane should indeed show stick-slip behavior (34,60,61).

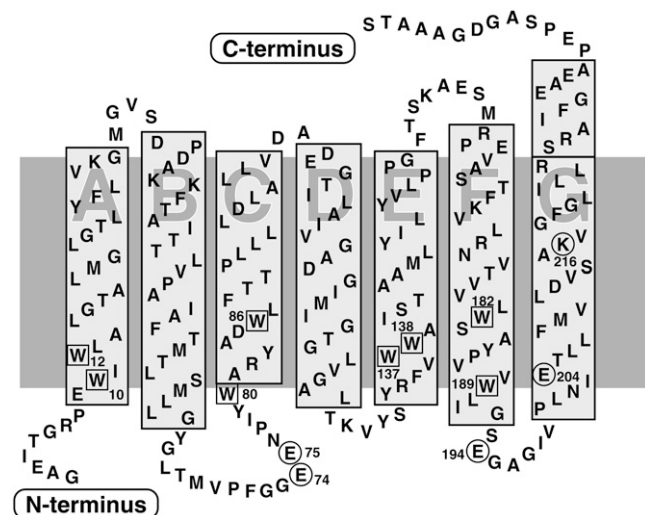


FIGURE 5 Scheme of bR aa sequence in the membrane (according to (14)). The Trp residues are boxed; Lys²¹⁶ (linking the retinal via a Schiff base) and the glutamates involved in extracellular ion binding are circled. The helices and the termini are labeled.

Possible steric contributions from other aromatic residues at low salt

Other bulky residues like Tyrosine (Tyr) and Phenylalanine could, in principle, also play a similar role to Trp in the steps observed at low salt concentration, and were suggested as an alternative explanation in previous studies (9,10). These residues are distributed, however, on both sides of bR (14,16) and cannot fully explain the unfolding steps. The most likely residue playing a role similar to Trp is Tyr because of its size and ability to form H-bonds (47,62). Mutation studies showed that Tyr⁵⁷ and Tyr⁸³ are important for bR function (63,64) and that they are involved in the retinal binding pocket (43). But no unfolding steps were observed around these positions at low salt concentration, apart from Tyr⁸³, which hydrogen-bonds with Trp¹⁸⁹ (14) and could be responsible for the step attributed to Trp⁸⁰.

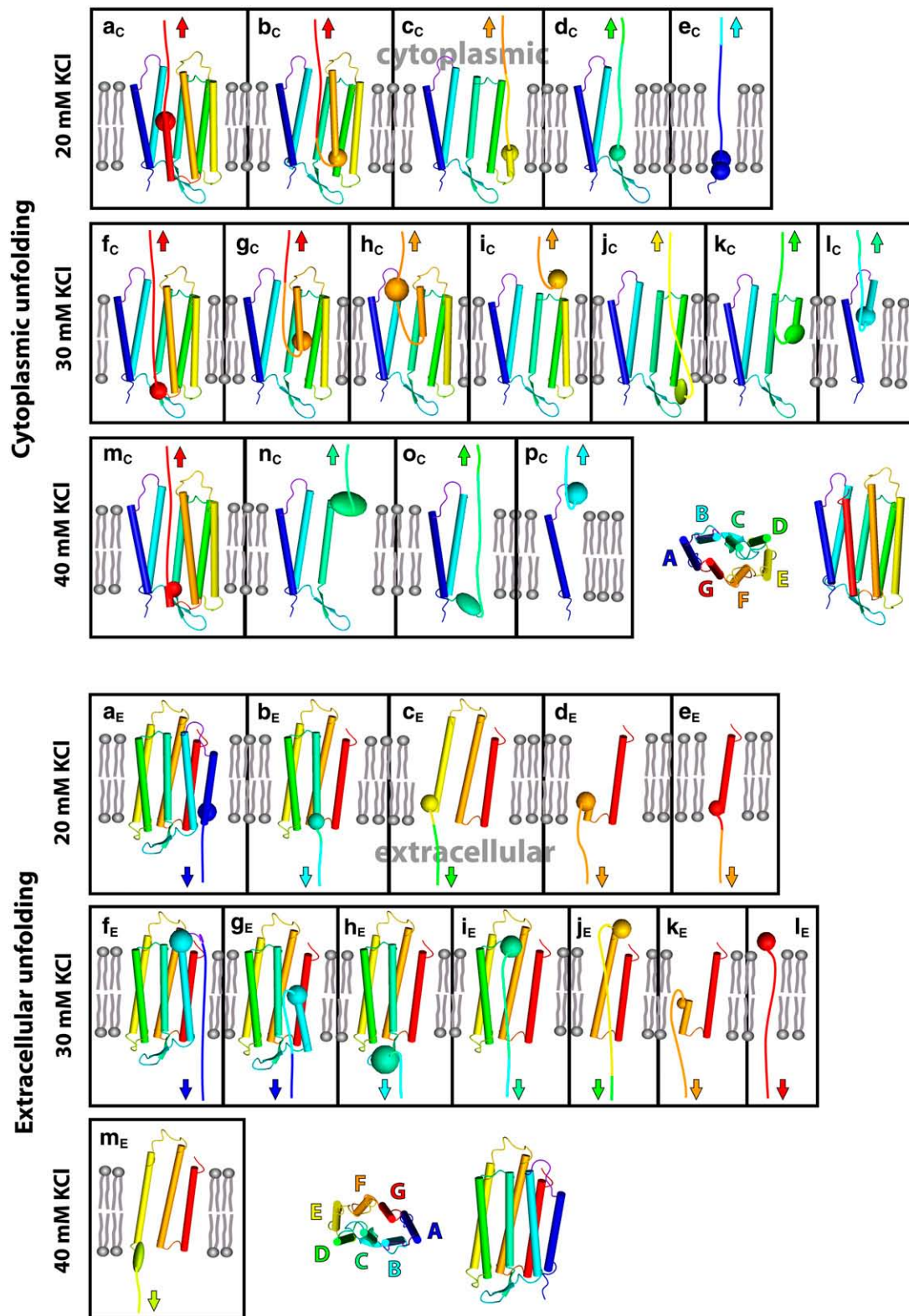


FIGURE 6 Scheme of the unfolding barrier positions reported in Table 2. The barriers are symbolized by a sphere or an ellipsoid fitting the residue(s) believed to be responsible for the step observed. At each salt concentration, the steps are classified following the order of the unfolding events (Fig. 3). The color of the arrows indicating the unfolding direction coincides with that of the structural element being unfolded. The color code used for bR helices is shown at the bottom (same color code as for Fig. 2). In each cartoon, the cytoplasmic side of PM is up, and the extracellular side is down. The extraction of both bR termini at 40 mM KCl (Table 2) is not shown.

Specific K⁺ binding to the Glu^{74–75} and Glu^{194–204} residues located on bR extracellular interhelical loops

When the salt concentration is increased from 20 mM KCl to higher salt concentrations, new unfolding steps are observed, some of which correspond to charged residue positions located on bR extracellular loops. The increased extracellular leaflet rigidity should favor ion binding to specific sites (48,56) by improving the stability of the electrostatic interactions. Both extracellular and cytoplasmic unfolding curves show some salt-dependent steps that can be attributed to bR extracellular loops (BC and FG for cytoplasmic curves and BC for extracellular curves, Table 2 and Fig. 6, f_C , m_C , o_C , e_E , and h_E). It has been shown that ions specifically bind to the bR extracellular side (65) and mutation studies have highlighted the interaction of Glu²⁰⁴ with Mn²⁺ ions (65) and proposed Glu⁹ and Glu^{194–204} as potential cation binding sites (66). The present data suggest that Glu^{74–75} and Glu^{194–204} offer specific binding sites for the K⁺ ions (see *circled residues* on Fig. 5). Glu¹⁹⁴ and Glu²⁰⁴ are involved in the proton release mechanism (67,68), and specific ion binding could enhance this release. Furthermore, specifically bound ions would support the formation of an extracellular network favoring lateral proton transfer toward proton sinks such as ATP-synthases (S. Antoranz Contera, K. Voitchovsky, and J. F. Ryan, unpublished, (69)).

The proximity of Trp^{10–12} from Glu⁹ and from the protein terminus does not allow an unambiguous conclusion about possible ion binding.

Secondary electrostatic unfolding barriers are mostly located in bR cytoplasmic region

Most of the remaining secondary barriers observed at 30 mM KCl and 40 mM KCl can be observed on both extracellular and cytoplasmic unfolding curves, except when they correspond to the different rearrangements of the protein fragments remaining in the membrane, which depend on the previous steps and therefore on the unfolding process. The barriers can be mainly classified in two categories, both consistent with enhanced electrostatic shielding within the cytoplasmic leaflet: extraction of looping helices perturbing a more cohesive cytoplasmic leaflet, and direct shielding of electrostatic repulsion by salt ions in the highly charged cytoplasmic loops.

Cytoplasmic curves obtained at 30 mM KCl show three steps corresponding to α -helix looping, two of which are confirmed in the extracellular curves: the first step corresponds to helix F looping around its natural hinge, Pro¹⁸⁶ (65) (Table 2 and Fig. 6 g_C), as predicted by simulation studies (70). The second step (Table 2 and Fig. 6 k_C), not observed on extracellular curves, corresponds to a location near Asp¹¹⁵, suggesting looping of helix D. The third step (Table 2 and Fig. 6 l_C) suggests helix B looping around Pro⁵⁰. The remaining steps can be explained by the extraction of the bulky Trp¹⁸⁹

from the cytoplasmic leaflet (Table 2 and Fig. 6 h_C), the resistance of the EF-loop (Glu¹⁶¹, Arg¹⁶⁴) (Table 2 and Fig. 6 i_C) and the rupture of interactions near the DE-loop (near Lys¹²⁹) (Table 2 and Fig. 6 j_C). This last step, also observed on extracellular curves at 40 mM KCl, is the only salt-dependent step corresponding to an extracellular location that cannot be explained by specific K⁺ binding to glutamates. Previous studies have proposed this step to be induced by multiple interhelical hydrogen bonds also involving Glu²⁰⁴ (10). However, since this step depends on salt concentration, the corresponding interaction involves ions. Lys²¹⁹ has indeed been shown to strongly influence the proton release through electrostatic interactions with its surrounding (71) and could be involved, with Glu^{74–75} and Glu^{194–204}, in the extracellular ion network mentioned above.

Extracellular curves obtained at 30 mM KCl show steps that coincide with the unfolding barriers identified on cytoplasmic curves except for three steps associated with locations on the highly charged AB- and CD-loops and near the cytoplasmic end of helix G (Table 2 and Fig. 6, f_E and i_E). The first two steps, also observed on cytoplasmic curves at 40 mM KCl, can be explained by the direct shielding of electrostatic interactions between charged residues (Asp^{36–38}, Lys^{40–41} and Asp^{101–103}, Glu¹⁰⁴, respectively). Several Asp and Arg and Glu residues located on these loops and on the EF-loop act as a proton-collecting antenna for bR proton pumping activity (17,72) and may form a salt-bridge network (70) responsible for the steps observed. The third step (Fig. 6 l_E), also reported in a previous study (10), has no equivalence on cytoplasmic curves and is consistent the extraction of Glu^{231–233–236} from the membrane.

Further increase of the ionic concentration to 40 mM KCl mostly reveals steps that confirm barrier locations already identified at 30 mM KCl (in Table 2 and Fig. 6: the steps m_C , n_C , o_C , p_C , and m_E observed at 40 mM KCl correspond to the 30 mM KCl steps e_E , i_E , h_E , f_E , and j_C , respectively). The only completely new steps correspond to the extraction of the bR C- and N-terminus, respectively. These last steps were poorly localized, however, and only observed for a small percentage of the curves (<10%).

Unfolding forces

The unfolding forces F_{unf} necessary to overcome the different unfolding barriers depend on the (steric/salt-dependent) nature of the barriers and are summarized in Fig. 3 and in Table 2. The unfolding force corresponding to a given barrier is more variable than the barrier's location, as visible in Fig. 3. This is because minor variations of many parameters such as the protein local conformation, the actual cantilever velocity, the local ionic concentration and temperature can influence the unfolding force without significantly modifying the corresponding barrier location (34). The force variation associated with each unfolding step represents the actual reproducibility of the unfolding mechanism and the relative

degree of variation of the protein local structure during the unfolding process.

At 20 mM KCl, cytoplasmic curves show well-characterized forces for each step at 144 ± 29 pN, 62 ± 17 pN, 101 ± 23 pN, 64 ± 35 pN, and 73 ± 13 pN, respectively (Figs. 1 and 3 and Table 2, a_C-e_C). This can be explained by the nature of the interactions involved: if steps are induced by the extraction of Trp residues, the corresponding specific steric interactions allow better force reproducibility than nonspecific electrostatic interactions. The location of the Trp residues also influences the unfolding process itself: when unfolding from the C-terminus, the membrane acts as a guide for the actual local pulling direction. In contrast, unfolding from the N-terminus will be more subject to local variations of the unfolding geometry. This is reflected by the poorer unfolding forces characterization showed by extracellular curves (138 ± 57 pN, 111 ± 41 pN, 109 ± 44 pN, 65 ± 34 pN, and 106 ± 35 pN) (Fig. 3 and Table 2, a_E-e_E).

At 30 and 40 mM KCl, the unfolding forces corresponding to the different steps show smaller variations (Table 2, f_C-p_C and f_E-m_E). This is because fewer steps are taken into consideration for the statistics (see the last part of Materials and Methods); this is clear in Fig. 3.

The forces associated with different unfolding steps tend to decrease as the protein unfolds (Fig. 3). This rule applies well to steps induced by nonspecific electrostatic shielding in the protein cytoplasmic region since the electrostatic repulsion vanishes as the protein is unfolded (e.g., $F_{\text{unf}}(f_E) > F_{\text{unf}}(i_E) > F_{\text{unf}}(j_E)$ at 30 mM KCl, Table 2). However, steps associated with steric specific interactions show many exceptions to this trend (e.g., Table 2, a_C-e_C).

Comparison with halorhodopsin

To test our hypothesis that Trp residues are responsible for the main unfolding barriers, we compared our results with the unfolding patterns reported for halorhodopsin (8), a similar seven-*trans*-membrane α -helix haloarchaeal protein acting as an inward light-driven chloride pump. Since halorhodopsin shows many structural, sequence (73) and dynamical (74) similarities with bR, the comparison is particularly relevant. The previously published halorhodopsin unfolding patterns, although not obtained in comparable ionic concentrations (300 mM KCl), reproducibly present four main distinct unfolding steps (8). Similarly to bR, halorhodopsin shows various more complex patterns where the main steps are still present (8). The halorhodopsin main unfolding pattern presents many similarities with that of bR and all the unfolding barriers reported can also be explained by the presence of a Trp residue (Trp²¹⁴, Trp¹⁵⁸, Trp¹⁰⁶, and Trp³⁴). For each step, our hypothesis coincides within 4 aa with the corresponding reported unfolding barrier location. The authors also point out one main difference with bR unfolding patterns, showing that helix E tends to unfold in multiple steps due to an unfolding barrier located near helix E cytoplasmic

extremity. Consistently with our model, halorhodopsin exhibits a Trp residue (Trp¹⁸³) located in this region, with no equivalent in bR (8,73).

Toward a functional description of bR interactions

Extracellular Trp steric and specific interactions constitute bR fundamental scaffolding and are therefore essential for the protein activity. The extracellular rigidity achieved through Trp interactions could play a dual role by supporting the retinal isomerization stereoselectivity (55) and by controlling the transmission of the photoinduced vibrational energy from the retinal to the protein (46,50). The vibrational energy transmitted allows the Schiff base deprotonation (45) by a partial disruption of the extracellular hydrogen-bond network (56). Furthermore, the vibrational energy could enhance the large conformational changes occurring in the softer cytoplasmic part during the second half of the photocycle (23,48,75) through amplification of the small vibration amplitude of the extracellular rigid network (76). The Trp scaffolding is indeed relatively static throughout the bR photocycle (48), allowing it to be anchored into the membrane through interactions with extracellular lipids known to be tightly and specifically bound to the protein (77,78). bR photocycle dynamics reflects its differential biomechanics: the retinal isomerization rapidly propagates within the extracellular part of the protein, allowing the proton release within <0.4 ms, while the reprotonation that takes part in the softer cytoplasmic region typically takes >10 ms (see, for example, (56)).

Direct interactions between bR monomers are weak (79), though, and to date, no direct interprotein interactions have been observed in bR unfolding patterns (35), regardless of photoinduced structural changes on the protein (9). The bR rigid and stable extracellular surface also offer ions specific locations to bind the loops, favoring the formation of an ordered layer of condensed counterions (S. Antoranz Contera, K. Voitchovsky, and J. F. Ryan, unpublished) that could support a rapid lateral migration of the released proton (69) toward proton sinks. The PM cytoplasmic leaflet is, on the other hand, governed by highly dynamical, nonspecific electrostatic interactions. bR cytoplasmic region is rich in charged residues acting as antennae for proton capture (72). Salt ions are necessary to screen mutual protein charge repulsion, but no ordered ionic layer can be established because of the dynamical nature of the electrostatic interactions involved (S. Antoranz Contera, K. Voitchovsky, and J. F. Ryan, unpublished). This allows the bR cytoplasmic-half to adapt structurally and dynamically throughout the photocycle to optimize proton uptake from the bulk and accommodate the large structural rearrangements necessary to reprotonate the chromophore (75,80).

Sources of error and implications in the results interpretation

The errors originating from the data analysis (procedures and attribution of the unfolding barriers) are discussed in Appendix C.

Once an unfolding barrier is attributed (as in Fig. 3; see also Materials and Methods and Appendices B and C) its biophysical interpretation is based on the corresponding location inside the protein and on the barrier nature (specific steric or electrostatic). In most cases, these two criteria are sufficient to unambiguously provide information about the mechanism for the barrier and/or about the aa involved. Previous studies employing other techniques could often further support our interpretation. Generally, the unfolding barriers attribution is less reliable at higher ionic concentrations (30–40 mM KCl), although it is clear that most of these barriers are located in the protein cytoplasmic region, apart for specific ion binding to the extracellular loops. At 20 mM KCl, however, most of the electrostatic interactions are suppressed, simplifying the problem; and the attribution of the steps to the Trp residues can be made with confidence. The dependence of these steps on the pulling parameters and comparison with halorhodopsin largely support this interpretation. Site-directed mutagenesis could, in principle, provide a further control, but most of the Trp mutations reported so far seriously affect the protein dynamics (43,50,81) and PM assembly (H. Besir and D. Oesterhelt, unpublished) (18). It is therefore likely that replacing Trp with smaller residues may dramatically alter the protein structure, making comparison with the native protein irrelevant.

CONCLUSIONS

Using side-specific single-molecule force spectroscopy of bR at different salt concentrations, we have been able to identify the nature and the aa involved in the different interactions dominating the protein local mechanical properties and function.

To survive in their extreme environment, PMs have developed a sophisticated strategy that exploits high ionic concentrations for enhancing bR activity. The protein extracellular and cytoplasmic regions present very different, yet complementary properties, the combination of which allows bR to function efficiently over a broad range of salt concentrations. Trp residues play a central role mainly by creating a rigid scaffold around the retinal and in the extracellular region of the protein, thus allowing efficient mechanical amplification of the chromophore photoisomerization while stabilizing, anchoring, and controlling the protein structure. Most of the archeal rhodopsins show a similar structure, with Trp enclosing the retinal and creating a network mainly in the extracellular region, suggesting the biomechanical strategy proposed for bR to be relevant for understanding the biomechanical basis of their respective function. Further to this common basis, each protein presents particular characteristics that depend upon its function and environment, such as specific extracellular ion binding sites for bR. Future molecular dynamics simulation of bR unfolding from PM will allow a detailed description of the role played by PM native lipids for anchoring and stabilizing bR.

APPENDIX A: IDENTIFICATION OF THE UNFOLDING BARRIER LOCATIONS USING THE WORMLIKE CHAIN MODEL

The wormlike chain model (WLC) relates the extension x of a flexible (bio-) polymer of contour length L to its persistence length A , the stretching force $F(x)$, and the thermal bath kT through the WLC equation (33):

$$F(x) = \frac{kT}{A} \left[\frac{1}{4} (1 - x/L)^{-2} - \frac{1}{4} + x/L \right].$$

This model assumes that entropic loss opposes the polymer resistance to stretching. Numerous studies have demonstrated the applicability of the WLC model in single protein unfolding (persistence length of 0.4 nm, amino-acid length of 0.36 nm) ((1,9) and references therein). Fitting the unfolding steps with the WLC equation allows the calculation of the unfolded contour length L_{out} (Fig. 2) at each step and therefore provides an estimate of the corresponding number of aa extended. Using high resolution crystallographic models of the protein (Luecke et al., model L (14) and Mitusoka et al., model M (16)) it is then possible to determine the particular location (along the protein aa sequence) of the unfolding barrier responsible for a given step (Table 2, Fig. 2). However, this procedure requires prior knowledge of the aa position from which the protein is actually unfolded (tip-binding shift; see Materials and Methods). This aa varies between the different curves due to nonspecific binding of the protein terminus to the tip. The curves were therefore aligned on one of the main unfolding steps visible at 20 mM KCl (third step when unfolding bR from the C-terminus and second step when unfolding from the N-terminus respectively, see Fig. 3, *a* and *d*, and Fig. 4, *a* and *d*). When unfolding bR from the C-terminus, we determined a global tip-binding shift for the aligned curves assuming that the first step observed (Fig. 3 *a*) corresponds to the position of the Lys²¹⁶ residue that binds the retinal. A barrier corresponding to this residue has been previously reported (9) and molecular dynamics simulations on bacterioopsin suggests that even without the retinal, a salt-bridges network involving Lys²¹⁶ would oppose unfolding (70). The unfolding barrier could also be justified by the retinal extraction from its rigid binding pocket. This attribution provides a shift of 18 aa or 20 aa, depending on the protein model used (Table 2). The global binding shift of the curves representing unfolding from the N-terminus was determined assuming that the second step observed at low salt (~ 77 aa; see Table 2) is triggered by the extraction of Trp⁸⁰ from the membrane (Table 2, Fig. 3 *d*). Trp⁸⁰ points away from the centre of the protein and is known to be important for maintaining PM native lattice assembly (18). Trp⁸⁰ has been suggested to interact specifically with the surrounding glycolipids (77), and its extraction from its natural location near the lipids carbonyl region is therefore expected to induce an unfolding barrier (34,57). The assessment of the second unfolding step to Trp⁸⁰ provided a shift value of 3aa to 4aa. This shift is compatible with the hypothesis that Trp^{10–12} are responsible for the first step within the fitting uncertainty of the WLC model (see Table 2 and Trp Residues Determine the Main Unfolding Steps through Specific Steric Interactions, in Discussion).

The determination of the unfolding barriers location inside bR could then be achieved assuming an aa length of 0.36 nm when extended (1) and of 0.15 nm when ordered in a α -helix (82), and full extension of the protein between a resisting unfolding barrier and the pulling AFM tip. The example provided in Fig. 2, *a* and *b*, uses the L-model (14) for bR structure. According to this model, a total of 14 aa are extended from 0.15 nm to 0.36 nm, thus inducing a measured extension $L_{\text{out}} = 14 \times (0.36 - 0.15 \text{ nm}) = 2.94 \text{ nm} \approx 8 \text{ aa}$ of the unfolded length (Fig. 2 *b*, Table 2).

The M-model (16) assumes that 2 aa are already extended outside the membrane when the unfolding begins (helix G ends at Ser²²⁶, see (16)), thus extending a total of 10 aa, which leaves a measured extension $L_{\text{out}} = 10 \times (0.36 - 0.15 \text{ nm}) + 2 \times 0.36 \text{ nm} = 2.82 \text{ nm} \approx 8 \text{ aa}$ (Table 2). The identification of the unfolding barrier rests on the implicit assumption that the unfolding process does not affect the structure of the protein still remaining

inside the membrane. In cases where the unfolding barrier was located at the opposite side of the membrane, L_{in} was assumed to be 11-aa long (see Fig. 2 *c*).

APPENDIX B: ANALYSIS OF THE UNFOLDING CURVES AND DETERMINATION OF THE BARRIER LOCATIONS

Analysis of the unfolding curves was performed by special routines programmed using Igor Pro. For each curve analyzed, the origin was first determined by fitting the curve with two articulated straight segments. The extremities of each segment were fixed to the extremities of the curve while the hinge point could run freely along the curve. The hinge point providing the best fit was retained as the new curve origin. A given set of unfolding curves could then be finely aligned on a particular step by minimizing the intercurve area within an adjustable region. At the lower salt concentrations (20 and 30 mM KCl), possible long-range repulsive forces (83) superimposed to the unfolding steps could be discriminated by subtracting a baseline obtained from corresponding extension curves. The unfolding step positions were then determined for each curve by considering variations of the first and second derivatives after smoothening. Different smoothening procedures were carried out in parallel (linear smoothening, local integration using a 0.7 nm window) and the results compared to ensure their reliability. The minimum between two successive steps could then be identified allowing determination of a relevant fitting interval for each unfolding step.

Each step in each curve was then fitted using the WLC model. The results obtained were added up to form three-dimensional statistical histograms of the step positions (in aa extended outside the membrane) versus the corresponding extraction force and the corresponding frequency (see Materials and Methods and Fig. 1 *c*). The results presented in Figs. 3 and 4 and in Table 2 are derived from the three-dimensional histograms data.

Due to bR unfolding patterns reproducibility, the statistical histograms exhibit local frequency maxima corresponding to particular protein extension lengths (e.g. in Fig. 1 *c* and Fig. 3). Such maxima were fitted with Gaussian distributions at each salt concentration (Fig. 3). It is clear when looking at the fitting distributions in Fig. 3 and the fitting examples in Fig. 4 that more unfolding steps appear as the salt concentration increases. Experimentally, we observed that unfolding steps present at a given salt concentration usually persist as the salt concentration increases. We used this last consideration as a fitting assumption throughout the analysis: before attributing new steps at a given salt concentration, we always excluded the possibility for the potential new step to be explained by an event already observed at a lower salt concentration. Steps depending on the salt concentration sometimes provide poorly reproducible locations (see Discussion and Appendix C), making it difficult to determine whether the attribution of a new step is fully justified. This is especially true when nonspecific electrostatic interactions are suspected to be responsible for the unfolding step. In the majority of cases, however, subjective choices could be excluded using the information overlap from the curves obtained by unfolding bR from both termini. Further support was also obtained by simply looking at the unfolding curves and considering possible structural justifications (Table 2). The reliability of the different step attributions and the corresponding implications in the results interpretation are discussed in detail in Discussion and in the Appendix C.

APPENDIX C: RELIABILITY OF THE ANALYSIS AND ERROR ESTIMATION

In the analysis procedure described above, there are two main sources of error that can influence the results and their interpretation:

1. The procedure described in Materials and Methods and in Appendix B aims at eliminating subjective interpretations of the results, first by analyzing the curves systematically with identical analysis parameters, and then by individually fitting every unfolding step that avoids possible

averaging effects. The procedure can, in principle, miss certain steps or report artifacts as unfolding steps. This is strongly limited, however, by the additional control procedures (described in Appendix B) and comparison of the results with the set of unfolding curves analyzed always showed a representative analysis of the data. A good example of the procedure robustness is displayed in Fig. 4: certain substeps have arguably been missed by the procedure, but all the main steps have been fitted. If some substeps are missed, the consequences will be equivalent for each salt concentration studied and will not introduce artifacts, but simply reduce the number of steps analyzed and consequently decrease some frequencies in the statistics.

2. The main source of error comes from the assignment of the different unfolding steps (derived from the frequency histograms in Fig. 3), especially for the higher ionic concentrations. However, the method employed to address this problem (see Materials and Methods and Appendix B) allows minimization of subjective decisions since it relies on the information gathered at a lower salt concentration where the step assessment is clearer, and provides a further control by comparing the unfolding barriers observable for cytoplasmic and for extracellular curves. Some isolated unfolding events (e.g., nonfitted spread peaks observed at 20 mM KCl for extracellular curves, Fig. 3 *d*) were not considered, especially if an increase in the ionic concentration produced far more events in this region, hence allowing a better analysis. The transition between the different ionic concentrations studied is continuous, and salt-related interactions cannot be excluded even at the lowest concentration. Increasing the number of curves analyzed could improve the assessment process, but the low unfolding probability (Table 1) made the acquisition of a substantially larger number of curves difficult. The consistent trend exhibited by the results obtained, the clear dependency of some unfolding barriers on the ionic concentration, and their respective location near highly charged residues often known to mediate important electrostatic interaction for the protein activity, support the results obtained and the corresponding interpretation. Furthermore, each set of curves shows the steps reported at 20 mM KCl as main unfolding events. These steps, reported in various previous experiments (3,5,9,10,35), are known to be associated with extracellular locations and can be considered as markers. The histograms presented in Fig. 3 then clearly confirm the appearance of salt-dependent unfolding barriers corresponding essentially to cytoplasmic locations, regardless of the detailed assessment of these steps.

Discussions with Dr M. R. R. de Planque are acknowledged.

This work has been supported by the Biotechnology and Biological Sciences Research Council, the Engineering and Physical Sciences Research Council, the Medical Research Council, and the Ministry of Defence through the Bionanotechnology Interdisciplinary Research Collaboration. K.V. acknowledges support from the Berrow Foundation through the Lord Florey scholarship.

REFERENCES

1. Rief, M., M. Gautel, F. Oesterhelt, J. M. Fernandez, and H. E. Gaub. 1997. Reversible unfolding of individual titin immunoglobulin domains by AFM. *Science*. 276:1109–1112.
2. Oberhauser, A. F., P. E. Marszalek, H. P. Erickson, and J. M. Fernandez. 1998. The molecular elasticity of the extracellular matrix protein tenascin. *Nature*. 393:181–185.
3. Oesterhelt, F., D. Oesterhelt, M. Pfeiffer, A. Engel, H. E. Gaub, and D. J. Müller. 2000. Unfolding pathways of individual bacteriorhodopsins. *Science*. 288:143–146.
4. Kedrov, A., C. Ziegler, H. Janovjak, W. Kuhlbrandt, and D. J. Müller. 2004. Controlled unfolding and refolding of a single sodium-proton antiporter using atomic force microscopy. *J. Mol. Biol.* 340:1143–1152.

5. Janovjak, H., M. Kessler, D. Oesterhelt, H. Gaub, and D. J. Müller. 2003. Unfolding pathways of native bacteriorhodopsin depend on temperature. *EMBO J.* 22:5220–5229.
6. Kedrov, A., M. Krieg, C. Ziegler, W. Kuhlbrandt, and D. J. Müller. 2005. Locating ligand binding and activation of a single antiporter. *EMBO Rep.* 6:668–674.
7. Janovjak, H., J. Struckmeier, M. Hubain, A. Kedrov, M. Kessler, and D. J. Müller. 2004. Probing the energy landscape of the membrane protein bacteriorhodopsin. *Structure.* 12:871–879.
8. Cisneros, D. A., D. Oesterhelt, and D. J. Müller. 2005. Probing origins of molecular interactions stabilizing the membrane proteins halorhodopsin and bacteriorhodopsin. *Structure.* 13:235–242.
9. Müller, D. J., M. Kessler, F. Oesterhelt, C. Möller, D. Oesterhelt, and H. Gaub. 2002. Stability of bacteriorhodopsin α -helices and loops analyzed by single-molecule force spectroscopy. *Biophys. J.* 83:3578–3588.
10. Kessler, M., and H. E. Gaub. 2006. Unfolding barriers in bacteriorhodopsin probed from the cytoplasmic and the extracellular side by AFM. *Structure.* 14:521–527.
11. Oesterhelt, D., and W. Stoekenius. 1971. Rhodopsin-like protein from the purple membrane of *Halobacterium halobium*. *Nat. New Biol.* 233:149–152.
12. Kates, M., S. C. Kushwaha, and G. D. Sprott. 1982. Lipids of purple membrane from extreme halophiles and of methanogenic bacteria. *Meth. Enzymol.* 88:98–111.
13. Corcelli, A., V. M. T. Lattanzio, G. Mascolo, P. Papadia, and F. Fanizzi. 2002. Lipid-protein stoichiometries in a crystalline biological membrane: NMR quantitative analysis of the lipid extract of the purple membrane. *J. Lipid Res.* 43:132–140.
14. Luecke, H., B. Schobert, H. T. Richter, J. P. Cartailler, and J. K. Lanyi. 1999. Structure of Bacteriorhodopsin at 1.55 Å resolution. *J. Mol. Biol.* 291:899–911.
15. Becker, O. M., Y. Marantz, S. Shacham, B. Inbal, A. Heifetz, O. Kalid, S. Bar-Haim, D. Warshaviak, M. Fichman, and S. Noiman. 2004. G protein-coupled receptors: in silico drug discovery in 3D. *Proc. Natl. Acad. Sci. USA.* 101:11304–11309.
16. Mitsuoka, K., T. Hirai, K. Murata, A. Miyazawa, A. Kidera, Y. Kimura, and Y. Fujiyoshi. 1999. The structure of bacteriorhodopsin at 3.0 Å resolution based on electron crystallography: implication of the charge distribution. *J. Mol. Biol.* 286:861–882.
17. Luecke, H., and J. K. Lanyi. 2003. Structural clues to the mechanism of ion pumping in bacteriorhodopsin. *Adv. Protein Chem.* 63:111–130.
18. Cartailler, J. P., and H. Luecke. 2003. X-ray and crystallographic analysis of lipid-protein interactions in the bacteriorhodopsin purple membrane. *Annu. Rev. Biophys. Biomol. Struct.* 32:285–310.
19. Lanyi, J. K. 1995. Bacteriorhodopsin as a model for proton pumps. *Nature.* 375:461–463.
20. Engel, M. B., and H. R. Catchpole. 2005. A microprobe analysis of inorganic elements in *Halobacterium salinarum*. *Cell Biol. Intl.* 29:616–622.
21. Madern, D., C. Ebel, and G. Zaccai. 2000. Halophilic adaptation of enzymes. *Extremophiles.* 4:91–98.
22. Oren, A., and L. Mana. 2004. Amino acid composition of bulk protein and salt relationships of selected enzymes of *Salinibacter ruber*, an extremely halophilic bacterium. *Extremophiles.* 6:217–223.
23. Voitchovsky, K., S. Antoranz Contera, M. Kamihira, A. Watts, and J. F. Ryan. 2006. Differential stiffness and lipid mobility in the leaflets of purple membranes. *Biophys. J.* 90:2075–2085.
24. Mitsui, K., M. Hara, and A. Ikai. 1996. Mechanical unfolding of α_2 -macroglobulin molecules with atomic force microscope. *FEBS Lett.* 385:29–33.
25. Kellermayer, M. S. Z., S. B. Smith, H. L. Granzier, and C. Bustamante. 1997. Folding-unfolding transitions in single titin molecules characterized with laser tweezers. *Science.* 276:1112–1116.
26. Carrion-Vazquez, M., P. E. Marszalek, A. F. Oberhauser, and J. M. Fernandez. 1999. Atomic force microscopy captures length phenotypes in single proteins. *Proc. Natl. Acad. Sci. USA.* 96:11288–11292.
27. Fisher, T. E., A. F. Oberhauser, M. Carrion-Vazquez, P. E. Marszalek, and J. M. Fernandez. 1999. The study of protein mechanics with the atomic force microscope. *Trends Biochem. Sci.* 24:379–384.
28. Li, H., A. F. Oberhauser, S. B. Fowler, J. Clarke, and J. M. Fernandez. 2000. Atomic force microscopy reveals the mechanical design of a modular protein. *Proc. Natl. Acad. Sci. USA.* 97:6527–6531.
29. Williams, P. M., S. B. Fowler, R. B. Best, J. Luis Toca-Herrera, K. A. Scott, A. Steward, and J. Clarke. 2003. Hidden complexity in the mechanical properties of titin. *Nature.* 422:446–449.
30. Cieplak, M., and P. E. Marszalek. 2005. Mechanical unfolding of ubiquitin molecules. *J. Chem. Phys.* 123:194903.
31. Möller, C., D. Fotiadis, K. Suda, A. Engel, M. Kessler, and D. J. Müller. 2003. Determining molecular forces that stabilize human aquaporin-1. *J. Struct. Biol.* 142:369–378.
32. Thompson, J. B., H. G. Hansma, P. K. Hansma, and K. W. Plaxco. 2002. The backbone conformational entropy of protein folding: experimental measures from atomic force microscopy. *J. Mol. Biol.* 322:645–652.
33. Bustamante, C., J. F. Marko, E. D. Siggia, and S. Smith. 1994. Entropic elasticity of λ -phage DNA. *Science.* 265:1599–1600.
34. Antoranz Contera, S., V. Lemaître, M. R. R. de Planque, A. Watts, and J. F. Ryan. 2005. Unfolding and extraction of a transmembrane α -helical peptide: dynamic force spectroscopy and molecular dynamics simulations. *Biophys. J.* 89:3129–3140.
35. Sapra, K. T., H. Besir, D. Oesterhelt, and D. J. Müller. 2006. Characterizing molecular interactions in different bacteriorhodopsin assemblies by single-molecule force spectroscopy. *J. Mol. Biol.* 355:640–650.
36. Kessler, M., K. E. Gottschalk, H. Janovjak, D. J. Müller, and H. E. Gaub. 2006. Bacteriorhodopsin folds into the membrane against an external force. *J. Mol. Biol.* 357:644–654.
37. Reference deleted in proof.
38. Butt, H. J., and M. Jaschke. 1995. Calculation of thermal noise in atomic force microscopy. *Nanotechnology.* 6:1–7.
39. Sader, J. E. 1995. Parallel beam approximation for V-shaped atomic force microscope cantilevers. *Rev. Sci. Instr.* 66:4583–4587.
40. Lehnert, U., V. Réat, B. Kessler, D. Oesterhelt, and G. Zaccai. 2002. Quantification of thermal motions in the purple membrane. *Appl. Phys. A.* 74:s1287–s1289.
41. Lee, A. G. 2003. Lipid-protein interactions in biological membranes: a structural perspective. *Biochim. Biophys. Acta.* 1612:1–40.
42. Biscan, J., N. Kallay, and T. Smolic. 2000. Determination of iso-electric point of silicon nitride by adhesion method. *Colloids Surf. A.* 165:115–123.
43. Mogi, T., T. Marti, and H. G. Khorana. 1989. Structure-function studies on bacteriorhodopsin. IX. Substitutions of tryptophan residues affect protein-retinal interactions in bacteriorhodopsin. *J. Biol. Chem.* 264:14197–14201.
44. Tuparev, N., A. Dobrikova, S. Taneva, and T. Lazarova. 2000. Bacteriorhodopsin thermal stability: influence of bound cations and lipids on the intrinsic protein fluorescence. *Zeitschrift für Naturforschung. C.* 55:355–360.
45. Wu, S., Y. Chang, M. A. el-Sayed, T. Marti, T. Mogi, and H. G. Khorana. 1992. Effects of tryptophan mutation on the deprotonation and reprotonation kinetics of the Schiff base during the photocycle of bacteriorhodopsin. *Biophys. J.* 61:1281–1288.
46. Schenkl, S., F. van Mourik, G. van der Zwan, S. Haacke, and M. Chergui. 2005. Probing the ultrafast charge translocation of photoexcited retinal in bacteriorhodopsin. *Science.* 309:917–920.
47. Petkova, A. T., M. Hatanaka, C. P. Jaroniec, J. G. Hu, M. Belenky, M. Verhoeven, J. Lugtenburg, R. G. Griffin, and J. Herzfeld. 2002. Tryptophan interactions in bacteriorhodopsin: a heteronuclear solid-state NMR study. *Biochemistry.* 41:2429–2437.
48. Réat, V., H. Patzelt, M. Ferrand, C. Pfister, D. Oesterhelt, and G. Zaccai. 1998. Dynamics of different functional parts of bacteriorhodopsin: H-²H labeling and neutron scattering. *Proc. Natl. Acad. Sci. USA.* 95:4970–4975.

49. Pebay-Peyroula, E., G. Rummel, J. P. Rosenbusch, and E. M. Landau. 1997. X-ray structure of bacteriorhodopsin at 2.5 Ångströms from microcrystals grown in lipidic cubic phases. *Science*. 277:1676–1681.
50. Rothschild, K. J., D. Gray, T. Mogi, T. Marti, M. S. Braiman, L. J. Stern, and H. G. Khorana. 1989. Vibrational spectroscopy of bacteriorhodopsin mutants: chromophore isomerization perturbs tryptophan-86. *Biochemistry*. 28:7052–7059.
51. Tsuda, M., M. Glaccum, B. Nelson, and T. G. Ebrey. 1980. Light isomerizes the chromophore of bacteriorhodopsin. *Nature*. 287:351–353.
52. Zgrablic, G., K. Voitchovsky, M. Kindermann, S. Haacke, and M. Chergui. 2005. Ultrafast excited state dynamics of the protonated Schiff base of all-trans retinal in solvents. *Biophys. J.* 88:2779–2788.
53. Nonella, M. 2000. Electrostatic protein-chromophore interactions promote the all-trans → 13-cis isomerization of the protonated retinal Schiff base in bacteriorhodopsin: an ab initio CASSCF/MRCI study. *J. Phys. Chem. B*. 104:11379–11388.
54. Becker, R. S., and K. Freedman. 1985. A comprehensive investigation of the mechanism and photophysics of isomerization of a protonated and unprotonated Schiff base of 11-cis-retinal. *J. Am. Chem. Soc.* 107:1477–1485.
55. Weidlich, O., B. Schall, N. Friedman, M. Sheves, J. K. Lanyi, L. S. Brown, and F. Siebert. 1996. Steric interaction between the 9-methyl group of the retinal and Tryptophan 182 controls 13-cis to all-trans re-isomerization and proton uptake in the bacteriorhodopsin photocycle. *Biochemistry*. 35:10807–10814.
56. Neutze, R., E. Pebay-Peyroula, K. Edman, A. Royant, J. Navarro, and E. M. Landau. 2002. Bacteriorhodopsin: a high-resolution structural view of vectorial proton transport. *Biochim. Biophys. Acta*. 1565:144–167.
57. de Planque, M. R. R., and J. A. Killian. 2003. Protein-lipid interactions studied with designed transmembrane peptides: role of hydrophobic matching and interfacial anchoring. *Mol. Membr. Biol.* 20:271–284.
58. de Planque, M. R. R., J. W. P. Boots, D. T. S. Rijkers, R. M. J. Liskamp, D. V. Greathouse, and J. A. Killian. 2002. The effects of hydrophobic mismatch between phosphatidylcholine bilayers and transmembrane α -helical peptides depend on the nature of interfacially exposed aromatic and charged residues. *Biochemistry*. 41:8396–8404.
59. de Planque, M. R. R., B. B. Bonev, J. A. A. Demmers, D. V. Greathouse, R. E. Koeppe, F. Separovic, A. Watts, and J. A. Killian. 2003. Interfacial anchor properties of tryptophan residues in transmembrane peptides can dominate over hydrophobic matching effects in peptide-lipid interactions. *Biochemistry*. 42:5341–5348.
60. Evans, E. 2001. Probing the relation between force, lifetime, and chemistry in single molecular bonds. *Annu. Rev. Biophys. Biomol. Struct.* 30:105–128.
61. Dudko, O. K., A. E. Filippov, J. Klafter, and M. Urbakh. 2003. Beyond the conventional description of dynamic force spectroscopy of adhesion bonds. *Proc. Natl. Acad. Sci. USA*. 100:11378–11381.
62. Hashimoto, S., M. Sasaki, H. Takeuchi, R. Needleman, and J. K. Lanyi. 2002. Changes in hydrogen bonding and environment of tryptophan residues on helix F of bacteriorhodopsin during the photocycle: a time-resolved ultraviolet resonance Raman study. *Biochemistry*. 41:6495–6503.
63. Mogi, T., L. J. Stern, N. R. Hackett, and H. G. Khorana. 1987. Bacteriorhodopsin mutants containing single tyrosine to phenylalanine substitutions are all active in proton translocation. *Proc. Natl. Acad. Sci. USA*. 84:5595–5599.
64. Faham, S., D. Yang, E. Bare, S. Yohannan, J. P. Whitelegge, and J. U. Bowie. 2004. Side-chain contributions to membrane protein structure and stability. *J. Mol. Biol.* 335:297–305.
65. Tuzi, S., J. Hasegawa, R. Kawaminami, A. Naito, and H. Saito. 2001. Regio-selective detection of dynamic structure of transmembrane α -helices as revealed from ^{13}C NMR. *Biophys. J.* 81:425–434.
66. Sanz, C., M. Marquez, A. Peralvarez, S. Elouatik, F. Sepulcre, E. Querol, T. Lazarova, and E. Padros. 2001. Contribution of extracellular Glu residues to the structure and function of bacteriorhodopsin: presence of specific cation binding sites. *J. Biol. Chem.* 276:40788–40794.
67. Balashov, S. P., E. S. Imasheva, T. G. Ebrey, N. Chen, D. R. Menick, and R. K. Crouch. 1997. Glutamate-194 to cysteine mutation inhibits fast light-induced proton release in bacteriorhodopsin. *Biochemistry*. 36:8671–8676.
68. Garczarek, F., L. S. Brown, J. K. Lanyi, and K. Gerwert. 2005. Proton binding within a membrane protein by a protonated water cluster. *Proc. Natl. Acad. Sci. USA*. 102:3633–3638.
69. Heberle, J., J. Riesle, G. Thiedemann, D. Oesterhelt, and N. A. Dencher. 1994. Proton migration along the membrane surface and retarded surface to bulk transfer. *Nature*. 370:379–382.
70. Seeber, M., F. Fanelli, E. Paci, and A. Caffisch. 2006. Sequential unfolding of individual helices of bacterioopsin observed in molecular dynamics simulations of extraction from the purple membrane. *Biophys. J.* 91:3276–3284.
71. Govindjee, R., E. S. Imasheva, S. Misra, S. P. Balashov, T. G. Ebrey, N. Chen, D. R. Menick, and R. K. Crouch. 1997. Mutation of a surface residue, Lysine-129, reverses the order of proton release and uptake in bacteriorhodopsin. Guanidine hydrochloride restores it. *Biophys. J.* 72:886–898.
72. Nachliel, E., M. Gutman, S. Kiryati, and N. A. Dencher. 1996. Protonation dynamics of the extracellular and cytoplasmic surface of bacteriorhodopsin in the purple membrane. *Proc. Natl. Acad. Sci. USA*. 93:10747–10752.
73. Blanck, A., and D. Oesterhelt. 1987. The halo-opsin gene. II. Sequence, primary structure of halorhodopsin and comparison with bacteriorhodopsin. *EMBO J.* 6:265–273.
74. Váró, G. 2000. Analogies between halorhodopsin and bacteriorhodopsin. *Biochim. Biophys. Acta*. 1460:220–229.
75. Vonck, J. 1996. A three-dimensional difference map of the N intermediate in the bacteriorhodopsin photocycle: part of the F helix tilts in the M to N transition. *Biochemistry*. 35:5870–5878.
76. Ferrand, M., A. J. Dianoux, W. Petry, and G. Zaccari. 1993. Thermal motions and function of bacteriorhodopsin in purple membranes: effects of temperature and hydration studied by neutron scattering. *Proc. Natl. Acad. Sci. USA*. 90:9668–9672.
77. Weik, M., H. Patzelt, G. Zaccari, and D. Oesterhelt. 1998. Localization of glycolipids in membranes by in vivo labeling and neutron diffraction. *Mol. Cell*. 1:411–419.
78. Henderson, R., J. S. Subb, and S. Whytock. 1978. Specific labeling of the protein and lipid on the extracellular surface of purple membrane. *J. Mol. Biol.* 123:259–274.
79. Isenbarger, T. A., and M. P. Krebs. 1999. Role of helix-helix interactions in assembly of the bacteriorhodopsin lattice. *Biochemistry*. 38:9023–9030.
80. Kamikubo, H., and M. Kataoka. 2005. Can the low-resolution structures of photointermediates of bacteriorhodopsin explain their crystal structures? *Biophys. J.* 88:1925–1931.
81. Soppa, J., J. Otomo, J. Straub, J. Tittor, S. Messen, and D. Oesterhelt. 1989. Bacteriorhodopsin mutants of *Halobacterium sp.* GRB II. Characterization of mutants. *J. Biol. Chem.* 264:13049–13056.
82. Eisenberg, D. 2003. The discovery of the α -helix and β -sheet, the principal structural features of proteins. *Proc. Natl. Acad. Sci. USA*. 100:11207–11210.
83. Müller, D. J., A. Engel, and M. Amrein. 1997. Adsorption of biological molecules to a solid support for scanning probe microscopy. *J. Struct. Biol.* 119:172–188.
84. Müller, D. J., J. B. Heymann, F. Oesterhelt, C. Möller, H. Gaub, G. Buldt, and A. Engel. 2000. Atomic force microscopy of native purple membrane. *Biochim. Biophys. Acta*. 1460:27–38.